# Synthetic Aperture Radar Imaging Using a Small Consumer Drone

Chenchen J. Li* and Hao Ling
Department of Electrical and Computer Engineering
The University of Texas at Austin
Austin, TX, USA

***Abstract*—Synthetic aperture radar (SAR) imaging is demonstrated using a small consumer drone. The entire imaging system including an ultra-wideband radar, antennas, and a single-board computer fits on a small drone and is controlled through a Wi-Fi connection. Motion compensation is carried out based on a prominent scatterer algorithm. The focused SAR image of four trihedrals is validated against simulation. Measured SAR images of a human and a car are also presented.**

## I. Introduction

There has been much recent interest in the use of small drones for aerial photography. This raises the possibility of using such small drones for synthetic aperture radar (SAR) imaging, which can offer complementary information and extended operating conditions in comparison to optical imagery. The use of large unmanned aerial vehicles (UAV) for SAR imaging is of course well established [1, 2]. The use of low-cost portable drones for radar imaging could open up other potential applications in scientific, agricultural, and environmental monitoring. In this work, we develop and demonstrate a low-cost SAR system mounted on a small consumer drone. The imaging system is comprised of an ultra-wideband radar connected to an on-board single-board computer with Wi-Fi capability. A Wi-Fi connection is used to remotely control the radar from a laptop on the ground. The entire system is mounted on the bottom of the small drone (see Fig. 1). By flying the drone in a straight line across the measurement scene, range profiles are collected continuously across different look angles of the scene. The data are then post-processed via motion compensation and inverse Fourier transform into SAR images.

## II. Measurement Synopsis

The measurement system consists of a portable radar, two antennas, a single-board computer with Wi-Fi capability, and a consumer drone. The radar is a Time Domain PulsON 410 ultra-wideband radar (P410). It emits short pulses at a pulse repetition frequency of 10 MHz with an equivalent frequency bandwidth from 3.1 to 5.3 GHz centered at 4.3 GHz. Two 5-turn helix antennas are used for transmit and receive. The radar sampling rate for consecutive range profiles is set at 20 Hz to provide sufficient pulse integration and range coverage. The radar is controlled via a Raspberry Pi Model B with a Wi-Fi dongle and is given instructions from a laptop over Wi-Fi. The entire system (including batteries and cables) weighs less than 300 g and is mounted to a DJI Phantom 2 drone. Range profiles

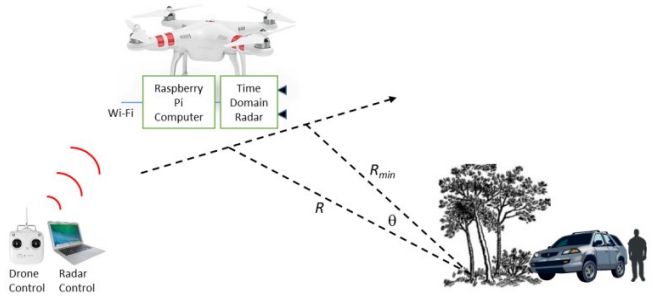


Fig. 1. Drone-SAR system and measurement setup.

are collected by flying the drone across the scene in a straight line (at approximately 2 m above the ground). The closest approach, $R_{min}$, is approximately 7.5 m. Fig. 1 shows a diagram of the measurement setup. Range profiles are collected over a distance of approximately 8 m or 60° of angular swath.

## III. Image Formation

For calibration and testing, four trihedrals (16 cm per side) are placed on the ground in a rhombus configuration with 3 m diagonals. Fig. 2(a) shows the measured range profiles vs. flight time. The four tracks in the plot correspond to the four trihedrals in the scene. As expected, the tracks exhibit significant range migration due to the wide angle collection. Fig. 2(b) shows the simulation result based on a point-scatterer model under a constant velocity flight. The same range tracks

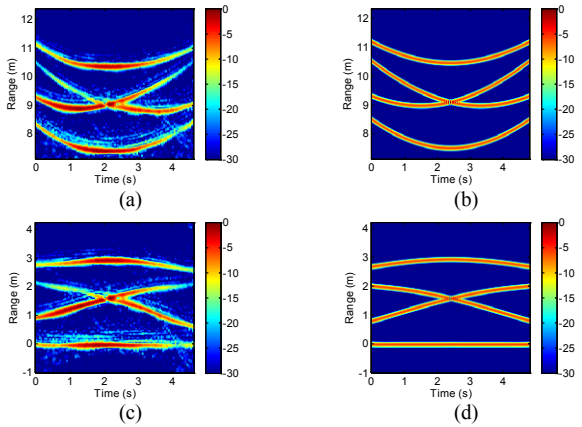


Fig. 2. (a) Measured range profiles vs. flight time from 4 trihedrals on the ground collected from the drone-SAR. (b) Simulated range profiles based on a point-scatterer model and constant velocity flight. (c) Aligned measured range profiles. (d) Aligned simulated range profiles.

are observed. To form an image from the data, translation motion compensation is first carried out by aligning to a prominent point-scatterer [3]. Fig. 2(c) shows the range profiles after range alignment to the closest trihedral. The center of rotation is now located at the closest scatterer. Again, good agreement with the aligned simulated range profiles in Fig. 2(d) is observed. Next, we perform rotation motion compensation to focus the scatterers located away from the rotation center. To accomplish this, we estimate the azimuth angle of the radar with respect to the rotation center and then apply $k$-space imaging. To relate measurement time with the azimuth angle $\theta$, we assume the flight path is straight and use the relationship $\theta = \cos^{-1}(R_{min}/R)$, where $R$ is the range at each instance in time, and $R_{min}$ is the minimum range (see Fig. 1). By applying a Fourier transform to the range axis, the range profiles vs. azimuth are transformed into frequency responses vs. azimuth. Based on the $k$-space imaging theory [4], a two-dimensional (2-D) image of the scene can be formed by a 2-D inverse Fourier transform of the collected frequency-azimuth backscattered data:

$$Image(r, cr) = \iint E^s(f,\theta)\, e^{jk_x r} e^{jk_y cr} dk_x dk_y \qquad (1)$$

$$k_x = (4\pi f/c)\cos\theta\,, k_y = (4\pi f/c)\sin\theta \qquad (2)$$

where $r$ is the down-range, $cr$ is the cross-range, $f$ is the frequency, $\theta$ is the azimuth angle, $E^s$ is the backscattered field as a function of frequency and azimuth, and $c$ is the speed of light. To speed up computation, the frequency-azimuth data are first interpolated onto a uniform $k_x$-$k_y$ grid, before applying the 2-D inverse fast Fourier transform to generate the SAR image.

## IV. Results

Fig. 3(a) shows the resulting SAR image based on the simulated point-scatterer data shown in Fig. 2(d). Three of the point-scatterers are well focused but the farthest point-scatterer exhibits some cross-range smearing. This is verified to be caused by near-field effects due to the closeness of the targets from the radar. Next, as an intermediate step, we mount the drone on a rail and smoothly move it along the measurement path. The resulting image is shown in Fig. 3(b). There is good agreement with the simulation; three of the trihedrals are well focused while the farthest trihedral exhibits some cross-range smearing. Finally, Fig. 3(c) shows the resulting SAR image from the drone flying along the measurement path. Other than the closest reference trihedral, the other trihedrals are less focused compared to Fig. 3(b) since the drone flight is not as smooth. Nonetheless, four trihedrals in their correct locations can be seen in the SAR image. Further correction of the near-field effect and the higher-order drone motion can be carried out using established algorithms [5, 6] to better focus the image.

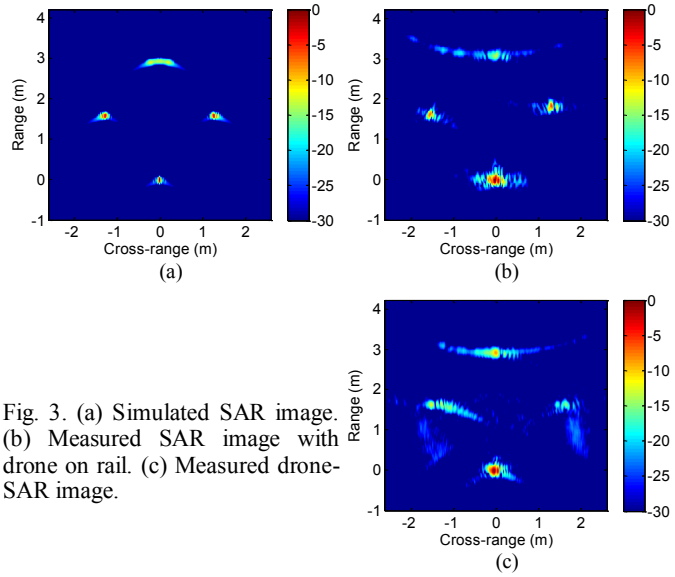


Fig. 3. (a) Simulated SAR image. (b) Measured SAR image with drone on rail. (c) Measured drone-SAR image.

SAR images of other targets in the scene are also formed. A trihedral is left in the scene for reference. Fig. 4(a) shows the SAR image of a stationary human. The focused point in front is the reference trihedral. Fig. 4(b) shows the SAR image of a car. The predominant contribution comes from the car side panel.

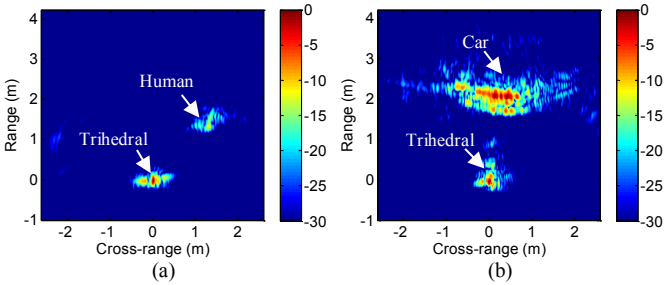


Fig. 4. (a) SAR image of a human. (b) SAR image of a car.

## V. Conclusion

We have demonstrated a low-cost, drone-based SAR imaging system. The entire system fits on a small consumer drone and can be controlled through a Wi-Fi connection. A SAR image of four trihedrals on the ground was formed using drone-collected measurement and a motion compensation algorithm. Additionally, SAR images of a human and a car were shown.


## Acknowledgment

The authors would like to thank Sam Grayson, Tiffany Dang, and Li Wang for their assistance. This work is supported in part by the National Science Foundation under Grant ECCS-1232152.


## References


[1] S. I. Tsunoda, F. Pace, J. Stence, M. Woodring, W. H. Hensley, A. W. Doerry, and B. C. Walker, "Lynx: A high-resolution synthetic aperture radar," in *IEEE Aerospace Conf. Proc.*, vol. 5, pp. 51-58, Mar. 2000.

[2] V. C. Koo, Y. K. Chan, V. Gobi, M. Y. Chua, C. H. Lim, C. S. Lim, C. C. Thum, T. S. Lim, Z. Ahmad, K. A. Mahood, M. H. Shahid, C. Y. Ang, W. Q. Tan, P. N. Tan, K. S. Yee, W. G. Cheaw, H. S. Boey, A. L. Choo, and B. C. Sew, "A new unmanned aerial vehicle synthetic aperture radar for environmental monitoring," *Progress Electromag. Research*, vol. 122, pp. 245-268, 2012.

[3] D. R. Wehner, *High Resolution Radar*, Norwood: Artech House, 1994.

[4] M. Soumekh, *Synthetic Aperture Radar Signal Processing with MATLAB Algorithms*, New York: Wiley, 1999.

[5] D. L. Mensa and K. Vaccaro, "Near-field to far-field transformation of RCS data," in *Proc. AMTA Symp.*, pp. 155-161, Nov. 1995.

[6] V. C. Chen and H. Ling, *Time-Frequency Transforms for Radar Imaging and Signal Analysis*, Norwood: Artech House, 2002.